Above-threshold ionization of argon with ultrashort orbital-angular-momentum beams

Arnab Sen,[1] Abhisek Sinha,[2] Sanket Sen,[2] V. Sharma,[2,*] and R. Gopal[3,†]
[1]*Indian Institute of Science Education and Research, Pune 411008, India*
[2]*Indian Institute of Technology Hyderabad, Kandi 502285, India*
[3]*Tata Institute of Fundamental Research, Hyderabad 500046, India*

(Received 3 May 2022; accepted 28 July 2022; published 5 August 2022)

Light-matter interaction with laser pulses endowed with orbital angular momentum (OAM) raises a fundamental question about the nature of the transfer of this property of light to matter. In this work, a "reaction microscope" is used for precise measurement of the momentum of ionized photoions and photoelectrons from the interaction of Ar atoms with a linearly polarized, ultrashort (∼25 fs), moderately intense (10^{13}–10^{14} W/cm^2) OAM carrying laser pulses. The angle and energy-resolved photoelectron spectrum is compared with the photoelectron spectrum obtained from the interaction with the laser beams with no OAM at similar intensities. No evidence of angular momentum transfer to the electrons from light is observed in our experiment.

DOI: 10.1103/PhysRevA.106.023103

I. INTRODUCTION

In the presence of a strong laser field an electron can be easily removed from an atom or molecule with absorption of multiple photons over the ionization threshold. This ionization mechanism is known as above-threshold ionization (ATI) [1]. Usually nonresonant ATI takes place through multiphoton absorption involving several intermediate virtual states when the Keldysh parameter γ is greater than 1 [2]. Here $\gamma = \sqrt{I_p/2U_p}$ with ionization potential I_p and ponderomotive energy $U_p = I_0/(4\omega^2)$, I_0 being the peak laser intensity and ω the laser frequency in atomic units. Modulations in magnitudes of the the momentum and angular distribution of the photoelectrons emerging through this nonresonant ionization process are understood as interferences between the photoelectron "trajectories" [3,4]. As these trajectories occur periodically across multiple laser cycles, peaks in the energy spectrum with periodicity of $\hbar\omega$ are expected. An associated effect of strong field ionization is the Stark-effect shifting of Rydberg states, which could be resonantly excited via multiphoton absorption. So a different pathway to ionization takes place through the absorption of a few more photons following this excitation. This ionization process via resonantly excited Rydberg states is known as Freeman resonance [5]. The photoelectrons ejected through Freeman resonance exhibit several substructures in the low-energy ATI peaks in the kinetic energy and momentum spectrum. The angular momentum quantum number of these resonant Rydberg states are reflected through the angular distribution of these photoelectrons [3,6]. Furthermore, an interesting radial fanlike pattern is observed in the 3D momentum spectra below the first-order nonresonant ATI peaks in several experimental and theoretical calculations [3,7]. These fanlike radial patterns of near-threshold photoelectrons emerge from the interference between trajectories of the low-energy electrons scattered due to the combined atomic potential and the laser field, also referred to as generalized Ramsauer-Townsend (GRT) diffraction oscillations [8]. The rich features of ATI have been studied in various conditions, experimentally and theoretically [9–13]. Experimental studies on ATI including the effect of wavelength [14], combination of wavelengths [15], intensity and pulse duration [16], polarization [17], carrier envelope phase [18], and initial spin and angular momentum state of the bound electron [19] have showed how the ATI spectra are closely related to these parameters.

Photon distributions can be endowed with an orbital angular momentum (OAM) [20] along with the spin angular momentum (SAM). The OAM carried by photons is closely related to its spatial phase distribution, in contrast to its SAM, which is related to the polarization. These special photons distributions can be generated in several ways, such as spiral phase plates, computer-generated holograms, integrated ring resonators, etc. [21–23]. The availability of OAM beams has opened up a wide range of experimental possibilities to understand the influence of the OAM carried by the photon beam [24]. Applications of such structured beams abound in optical manipulation [25,26], astrometry [27], and microscopy and imaging [28,29]. Experiments which probe the interaction of OAM photons with pointlike particles (dimensions far less than the wavelength) are few and portray the inherent contradictions in understanding the transfer of the angular momentum of light to matter and if OAM is an intrinsic attribute of light. Giammanco *et al.* [30] could not find evidence of such transfer in dipole-allowed transitions [31] in a Rb gas cell, On the other hand, in quadrupole electronic excitation of trapped $^{40}Ca^+$ ions [32] modification of the selection rules is observed at the strong transverse field gradients near the amplitude nodes of the structured beams, interpreted as OAM transfer.

In the strong field regime, pioneering theoretical investigations [33,34] pointed out that the selection rules for the

*vsharma@phy.iith.ac.in
†ramgopal@tifrh.res.in

excitation and ionization of the atoms can be different for beams carrying OAM than plane waves owing to the transfer of OAM to the atomic system. Subsequent works have explored the angular distribution of the electrons emitted during the course of photoionization by the OAM beams [35]. No effect of the helical phase structure of the beam on photoelectrons emitted in the plane perpendicular to the propagation direction of the laser beam was seen. In the perpendicular direction, however, the electrons are found to carry significant momenta [36] with distinct ATI peaks [37]. However, in experimental conditions, with a cloud of atoms the measured momentum distribution would be dominated by photoelectrons released in the most intense parts of the laser beam, wherein negligible OAM transfer is predicted [38]. Yet in a strong field-driven process like high-order harmonic generation from the interaction with OAM carrying laser pulse, each harmonic was found to carry topological charge $q\ell$, where q is the order of the harmonic and ℓ is the intrinsic orbital angular momentum carried by the fundamental driving beam [39–42]. The high-order harmonic helical beams are understood to result from the far field interference of single atom sources emitting with the phase characteristics of the driving laser field. This highlights the need for coherent addition of the single atom responses over the annular interaction region for high harmonic generation [43]. However, in strong field ionization, the single atom responses are added up incoherently [44]. Experimental studies on strong field-driven ionization using NIR OAM laser beams are sparse and very recent, typically involving assisted ionization from XUV [45] or visible (400 nm) [46] radiation. The ionized electron wave packets on the way to the detector interact with gradients in the electric field of the OAM beam.

In this work, we consider laser pulses with the transverse spatial structure represented by the Laguerre-Gaussian functions $\mathrm{LG}_{p,\ell}(\rho, \phi, z, \omega/c)$, also known as the Laguerre-Gaussian modes. The functional form of the transverse spatial structure of the Laguerre-Gaussian mode is written as

$$LG_{p,\ell}(\rho,\phi,z,\omega/c) = \sqrt{\frac{2p!}{\pi(|\ell|+1)!}}\frac{1}{w(z)}L_p^{|\ell|}\left(\frac{2\rho^2}{w^2(z)}\right) \times \left(\frac{\sqrt{2}\rho}{w(z)}\right)^{|\ell|}\exp\left(\frac{\rho^2}{w^2(z)}\right) \times \exp\left[i\ell\phi + i\frac{k_0\rho^2}{2R(z)} + i\Phi_G(z)\right],$$

where $\rho=\sqrt{x^2+y^2}$, $\phi = \arctan(y/x)$, k_0 is the carrier wave vector, $w(z) = w_0\sqrt{1+(z/z_0)^2}$ with w_0 is the width of the mode at $z = 0$, $R(z)$ is the phase front radius, z_0 is the Rayleigh range, $\Phi_G(z)$ denotes the Gouy phase, and $L_p^{|\ell|}$ are the associated Laguerre polynomials. The indices $p = 0$, 1, 2,...and $\ell = 0, \pm1, \pm2$,...indicate the nonaxial radial nodes and winding of the mode. This mode also includes a phase factor of $e^{i\ell\phi}$ giving rise to the discrete OAM of order $\ell\hbar$ per photon along the propagation direction [20]. The 3D momentum distributions of the photoelectrons from the interaction with moderately intense (10^{12}–10^{13} W/cm^2) OAM carrying laser pulses, $\mathrm{LG}_{0,1}$, with a cold supersonic jet of argon gas are precisely measured using a "reaction microscope." These distributions are compared with those obtained for beams with Gaussian (lowest order Hermite-Gaussian, $\mathrm{HG}_{0,0}$) spatial distributions at the same peak intensity levels. The comparison between the momentum distribution of the photoelectrons emerging from the interaction with plane wave laser pulse and OAM carrying laser pulse shows negligible difference for the resonant and the near-threshold electrons. In particular, through partial wave analysis of the momenta, no new components are observed. However, the yields for the nonresonant ATI electrons from OAM laser beams are lower relative to those obtained by $\mathrm{HG}_{0,0}$ beams, a possible consequence of the increased ionization volume

II. EXPERIMENTAL SETUP

A Femtopower V (Spectra-Physics, Austria) laser generates 25 fs, 1 kHz, 5 mJ pulses at 800 nm, a fraction of which is utilized on the atomic physics beamline. The polarization of the laser beam is linear and is set parallel to the spectrometer axis using a thin $\lambda/2$ plate (B-Halle, Germany). A thin $f =$ 30 cm lens focuses the laser onto the supersonic argon beam to a spot size (the diameter at half-maximum) of ~30 μm (for $\mathrm{HG}_{0,0}$) inside the chamber housing the spectrometer of the "reaction microscope."

A spiral phase plate (HOLO/OR Ltd.) is placed in the beam path to effect a (partial) conversion of the input laser beam Gaussian mode ($\mathrm{HG}_{0,0}$) to Laguerre mode ($\mathrm{LG}_{p,\ell}$). The orbital angular momentum carried by the output beam is $\ell = 0.95$, measured in an independent experiment by imaging the beam profile using a single cylindrical lens and a camera [47]. The spot size of the $\mathrm{LG}_{0,1}$ beam at the interaction region in the spectrometer is measured to be ~40 μm. The fused silica-made spiral phase plates cause a dispersive broadening of the transmitted pulse. A glass plate of similar thickness of the spiral phase plate is introduced to incorporate similar dispersive broadening in the $\mathrm{HG}_{0,0}$ beam path.

The "reaction microscope" used here is a coincident ion-electron momentum spectrometer measuring all three-momentum components of the charged particles [48]. Argon atoms at a stagnant pressure of ~0.5-1 bar are forced through a nozzle of ~30 μm diameter into vacuum, and hence the atoms are accelerated to supersonic speeds causing an effective cooling of the internal motion. Two cone-shaped skimmers of a ~280 μm diameter are placed behind the nozzle and between the two pumping stages before the reaction chamber to extract a geometrically well-defined and cold argon beam. The pressure in the reaction chamber is below 10^{-8} mbar. The spectrometer consisting of a series of parallel plates coupled with a resistor chain is placed in the reaction chamber and used to accelerate the ions and electrons to their respective detectors placed opposite each other. The laser pulses with polarization parallel to the spectrometer fields are focused into the jet, causing ionization. The ionized ions and electrons are accelerated by ~1.5 V/cm electric fields and confined by ~10 G magnetic fields, which allow us to collect the electrons with the maximum transverse momentum up to ~0.4 a.u. with a 4π solid angle. The detector is a microchannel plate followed by a delay line-type position sensitive anode (Roentdek GmbH, Germany) to provide 2D position and flight time of each of the ions and electrons in a list mode fashion. With the

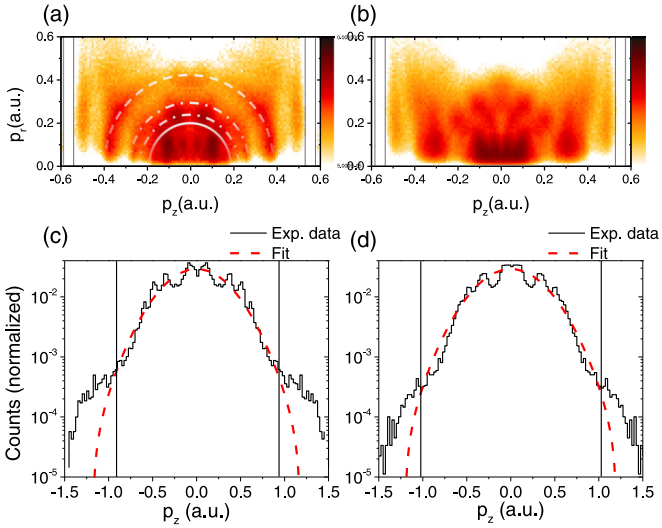

FIG. 1. 2D photoelectron momentum distribution with horizontal axis p_z being parallel to the laser polarization direction and the vertical axis being the transverse momentum in a plane perpendicular (p_r) to the laser polarization direction. The photoelecteons emerge from interaction of argon with $HG_{0,0}$ beams at (a) 90 TW/cm^2 and (b) 105 TW/cm^2 intensities. Vertical cuts (near $\sim\pm$ 0.6 a.u.) show regions where the spectrometer has no resolution in the transverse direction. The lower panels (c, d) are projections of the above momentum distributions along p_z. The vertical lines are to identify the start of the plateau region electrons.

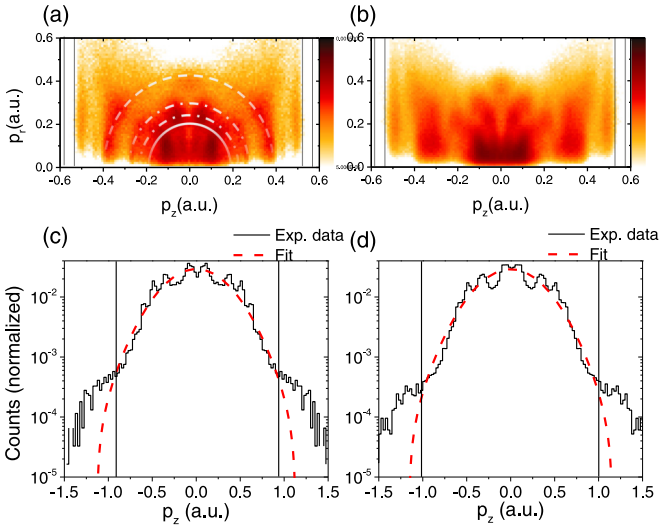

FIG. 2. Same as Fig. 1 showing the photoelectrons emerging from the interaction of argon atoms with $LG_{0,1}$ beams at (a, c) 90 TW/cm^2 and (b, d) 105 TW/cm^2.

time-of-flight and position information, one can have the complete momentum distribution of the above-threshold ionization. The average ion/electron count rates ($\sim$100–500 Hz) were such that, statistically, less than one ionization event occurred per laser pulse interaction. Under these experimental conditions the measured momentum resolution obtained from the sum of the longitudinal component (along the spectrometer axis) of the ion and electron momentum is $\sim\pm 0.06$ a.u. The electron spectrometer resolution along this axis is estimated to be $\sim\pm 0.01$ a.u. The transverse momentum resolution is estimated as $\sim\pm 0.05$ a.u. [49]. Each data set for different intensities of $HG_{0,0}$ and $LG_{0,1}$ is recorded for 6 h.

III. RESULTS AND DISCUSSION

Figures 1(a) and 1(b) show the 2D momentum distribution of the photoelectrons emerging from the interaction of argon atoms with $HG_{0,0}$ beams at intensities of 90 TW/cm^2 and 105 TW/cm^2, respectively.

The corresponding 1D electron momentum distributions, p_z, projected to the axis parallel to the laser polarization axis are plotted in Figs. 1(c) and 1(d). The laser peak intensity is estimated by identifying the beginning of the plateau [marked by straight lines in Figs. 1(c) and 1(d)], which indicates the maximum drift momentum the electron can gain from the laser field classically, $2\sqrt{U_p}$ [7]. Here U_p, the ponderomotive energy, is the cycle-averaged quiver energy of a free electron in the laser field. A Gaussian fit to the 1D distribution of the drift momentum of the direct electrons is overlaid as an empirical aid to distinguish the direct electrons from the rescattered photoelectrons. The point of deviation of the fit from the experimental data is consistently chosen as the maximum drift momentum of the direct electrons $2\sqrt{U_p}$. The estimated uncertainty of the calibrated laser intensity is less than $\pm$5%. The vertical and horizontal axes in Figs. 1(a) and 1(b) show the longitudinal (p_z along the spectrometer axis) and transverse electron momenta (p_r perpendicular to the spectrometer axis) in a range from -0.6 to $+0.6$ a.u. and 0.0 to $+0.6$ a.u., respectively.

Three major segments can be distinguished from the 2D photoelectron momentum spectrum shown in Fig. 1(a). The photoelectrons with higher momentum ($|p| \geqslant 0.3$ a.u.) highlighted by a dashed semicircle show an anisotropic distribution peaking at $|p| = 0.37$ a.u. A similar structure, albeit with lower counts, is seen at $|p| = 0.5$ a.u. The energy difference between the two peaks of $\approx$1.55 eV suggests these electrons to be due to nonresonant ATI. Two dashed semicircles, highlighting the photoelectrons with |p| $\sim$ 0.26 a.u. and $\sim$0.22 a.u., exhibit several ringlike structures with an oscillatory pattern. These are indicative of resonance-enhanced ionization via intermediate Rydberg states of the argon atom, that is, Freeman resonances. The solid semicircle demarcates low-energy photoelectrons with $|p| \leqslant 0.17$ a.u. These low-energy photoelectrons form a fanlike structure, similar to the GRT interference fringes.

The 2D-momentum distributions of the photoelectrons recorded for the interaction of argon atoms with the $LG_{0,1}$ beams show similar distributions as observed in the interaction with $HG_{0,0}$ beams (see Fig. 2). The intensity regime of the $LG_{0,1}$ laser pulses is matched to the intensity regime of the $HG_{0,0}$ beam by appropriately choosing the power, confirmed by checking the beginning of the plateau in the ion momentum distribution. The three major segments corresponding to near-threshold ionization, resonant, and nonresonant ionization processes are highlighted in the same manner over the 2D-momentum distribution. These features in the spectra are analyzed as a function of increasing peak intensity in the following sections.

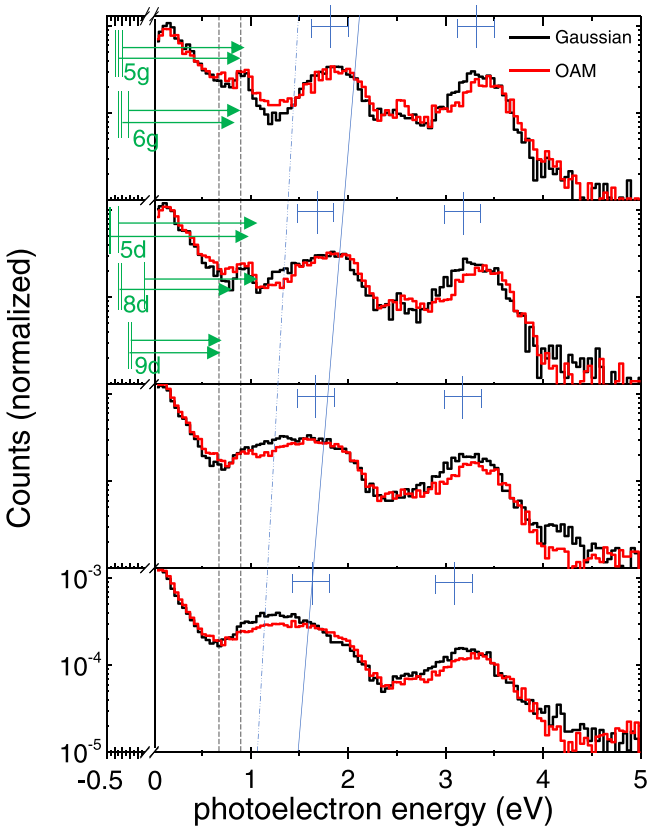

FIG. 3. Normalized (total counts) photoelectron energy spectra at different intensities of 90 TW/cm^2, 95 TW/cm^2,100 TW/cm^2, and 105 TW/cm^2. The tilted solid lines indicate the expected position of the ATI peak with a 15-photon absorption at the peak intensity. The tilted dotted line shows the expected position of the ATI peak including the focal volume effect with 13-photon absorption. The cross hairs with error bars indicate the peak positions of the nonresonant ATI peaks in the photoelectron spectra. Higher-lying Rydberg states are shown with solid horizontal lines in the negative energy scale to highlight the possible resonant ionization processes. The intensity-independent structures from resonant ionization through Rydberg states are marked with dashed-dot lines.

A. Resonant and nonresonant ionization

In general, the electron energy peaks due to nonresonant ionization shift towards the lower energy side with increasing peak intensity due to an ac Stark shift of the ionization threshold. The effective ionization potential increases by U_p, and the expected ATI peaks follow the following relation:

$$E_k = n\omega - (I_p + U_p), \tag{1}$$

where n is number of photons absorbed by the argon atom during the ionization process. Such a shift in energy is seen for the electrons from 1.85 eV (p| $\sim$ 0.37 a.u.) to 1.25 eV (see Fig. 3). This feature therefore can be associated with a nonresonant ATI process [50]. The intensity dependence could also be used to calibrate the peak intensity of the laser pulse. The recorded peak shift of this nonresonant ionization agrees well with our estimated peak intensity by measuring the beginning of the plateau as elaborated in the preceding sections.

The photoelectron distribution through the resonant ionization shows many pronounced ringlike structures in the 2D photoelectron momentum spectrum. Figures 1(a), 1(b), and 2 indicate two prominent intensity-independent ringlike structures at 0.75 ± 0.05 and 0.93 ± 0.05 eV. These structures are assigned to resonantly enhanced multiphoton ionization through the Rydberg states By comparing the peak positions with the available data of argon atom [51], the possible resonant intermediate state at the peak intensity of 90 TW/cm^2 is assigned. In the multiphoton absorption picture, energy corresponding to an integer number of photons is absorbed to excite the electrons from the ground state to a Rydberg state. The atom excited to a Rydberg state will absorb an extra photon to reach the continuum. For an intermediate Rydberg state with angular momentum of l, the angular momentum in the continuum following one photon ionization from this state could be either $l-1$ or $l+1$. Theoretical investigations predict the transition matrix element for l to $l+1$ transition to be greater than the transition matrix element for l to $l-1$ transition [52]. It should be noted, however, that several experimental results show that this is not always the case [53,54]. Only a few Rydberg states will satisfy the resonant condition at a certain intensity value due to the ac Stark shift in the Rydberg state. However, considering the extended source of photoelectrons through the intersection of the finite gas jet with the focal volume of the laser beam in the experiment, such resonant ionization can occur over a broad range of peak laser intensities. Furthermore, due to dipole parity selection rules, the excitation to p and f states requires an even number of photons. Similarly excitation to s, d, and g states follows the absorption of an odd number of photons from the ground state of argon [55]. Possible resonant ionization processes through various Rydberg states are highlighted in Fig. 3.

The photoelectron angular distribution (PAD) of these resonant structures can be expressed as [3]

$$\frac{d^2P}{dEd(\cos\theta)} \approx [P_l(\cos\theta)]^2, \tag{2}$$

where E denotes the photoelectron energy. A single Legendre polynomial corresponds to the dominant contributing partial wave for the angular distribution. Usually the number of peaks in the PAD is determined by the dominant angular momentum; however, the contributions from other partial waves could be also significant. To incorporate the contributions from other partial waves, the recorded PAD is fitted with $\Sigma_l C_l[P_l(\cos\theta)]^2$, which includes different l values from 0 to 6. The fitted distributions show good agreement with the experimental data, and the contribution from each l value for various intensities are shown in Figs. 4(a) and 4(b).

Figure 4(a) shows the fitted angular distribution, and the corresponding contributions from different partial waves for the resonant ionization channel 0.75 ± 0.05 eV are plotted in Fig. 4(c). The partial waves of degrees 0 and 5 have a dominant contribution for this channel. Energy-level analysis suggests that the Rydberg state $6g$ via $13+1$ photon ionization process could be responsible for the dominance of angular momentum value 5. However, no appropriate transient Rydberg states are found from the energy-level analysis to correspond to the p state, which explains the partial waves of degree 0.

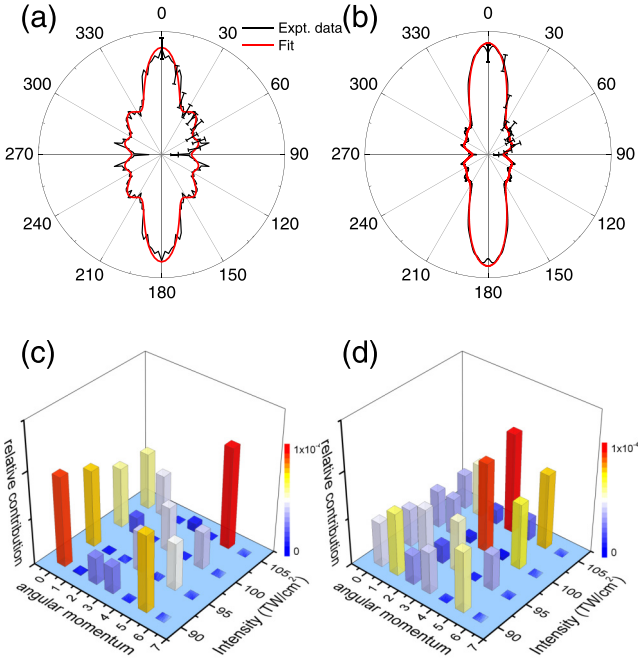

FIG. 4. Photoelectron angular distributions (PADs) of the resonant structures (a) $(0.75 \pm 0.05\,\mathrm{eV})$ and (b) $(0.93 \pm 0.05\,\mathrm{eV})$ at peak intensity $\sim 105\ \mathrm{TW/cm^2}$ are fitted with Legendre polynomial up to order $l = 6$, and the contribution of individual terms are is shown in (c) and (d) as a function of peak intensity of the $HG_{0,0}$ beam, respectively.

The resonant structure plotted in Fig. 4(b) highlights the photoelectrons emerging with energy $0.93 \pm 0.05\,\mathrm{eV}$. The partial waves of degree 3 and 5 are significant in the observed PAD of the associated photoelectrons [Fig. 4(d)]. The relative contribution of these partial waves shows no change with increasing intensity. The dominant partial waves indicate the intermediate resonant electronic state could be from $5g$ via $13 + 1$ photon ionization, which also supports the energy level calculation.

B. Near-threshold electrons

The near-threshold photoelectrons exhibit a fanlike pattern inside the dashed circle ($\sim$0.4 eV) shown in Fig. 1. The angular distribution of these near-threshold photoelectrons recorded for intensities between 90 $\mathrm{TW/cm^2}$ and 105 $\mathrm{TW/cm^2}$ are again fitted with $\Sigma_l C_l [P_l(\cos\theta)]^2$ incorporating multiple partial waves up to order 6. The fitting shows a good agreement with the observed data. Figure 5(a) indicates that three partial waves of degree 0, 1, and 5 have dominant contribution, which remain independent of intensity. The parent states for the low-energy electrons might arise from s, p, and g states, respectively. The energy-level analysis indicates that electrons with $\sim$0.2 eV could arise from an intermediate resonating Rydberg state $5p$ via 12 photon resonance. However, in this intensity regime, no intermediate s or g states are found to be involved from the energy-level analysis.

Classical-trajectory Monte Carlo calculations show the near-threshold photoelectrons could arise from the interference between different trajectories of the low-energy photoelectrons with the laser field as well as the Coulomb potential of the parent ion [3,56]. Hence, the angular distribution of these near-threshold photoelectrons could be highly influenced by the Coulomb potential of the parent ion and the nature of the laser field. The dominant angular momentum carried by the photoelectrons can be estimated analytically [56]:

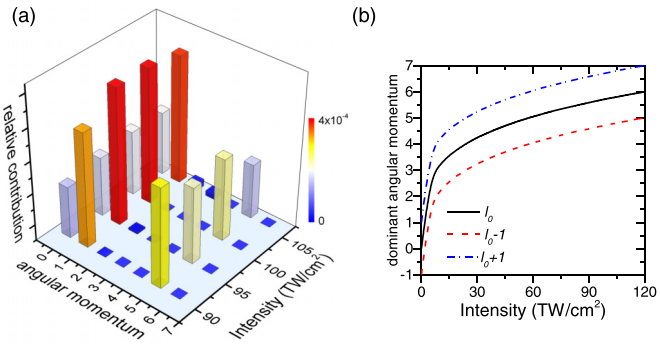

FIG. 5. (a) Same as Fig. 4, but for near-threshold photoelectrons as a function of peak intensity of the Gaussian beam. (b) The dominant angular momentum of the near-threshold photoelectrons as a function of peak intensity of the Gaussian beam. The black solid line indicates the semiclassical result. The dashed red and the dashed-dot blue lines highlight the uncertainty region due to quantum discreteness.

$$l_0 = (2Z_T\alpha)^{1/2}, \tag{3}$$

where l_0 is the dominant classical angular momentum, Z_T is the residue charge in the parent atom after the ionization takes place, and $\alpha = F_0/\omega^2$ is the electron quiver amplitude in the laser field with the amplitude F_0 and the frequency ω. The estimated angular momentum of these near-threshold photoelectrons is 5 in the intensity regime 90–110 $\mathrm{TW/cm^2}$. The contribution of angular momentum $l_0 = 5$ is also observed in our experiment [see Fig. 5(b)]. This explains a significant portion of the near-threshold photoelectrons arising through the nonresonant process and under the combined effect of Coulomb potential and the laser field [57], i.e., the GRT diffraction oscillations. The remnant contribution from $l = 0$ electrons could be surmised to arise from nonresonant above-threshold ionization, which is also energetically expected.

C. Interaction with OAM beams

The 2D-momentum distributions of the photoelectrons recorded for the interaction of argon atoms with the $LG_{0,1}$ beams show similar distributions as above (see Figs. 6 and 7). The peak intensities of the $LG_{0,1}$ laser pulses are the same as those of the $HG_{0,0}$ beams and are confirmed by checking the beginning of the plateau in the ion momentum distribution and the shift in the nonresonant ATI peak with intensity. It must be stated that the total energy in the laser beam is considerably higher (factor of $\sim$1.8) for the $LG_{0,1}$ to match the intensities. So the count rates are also significantly higher in the $LG_{0,1}$ experiments. The normalized distributions shown here are with respect to the integral number of counts in each experimental run.

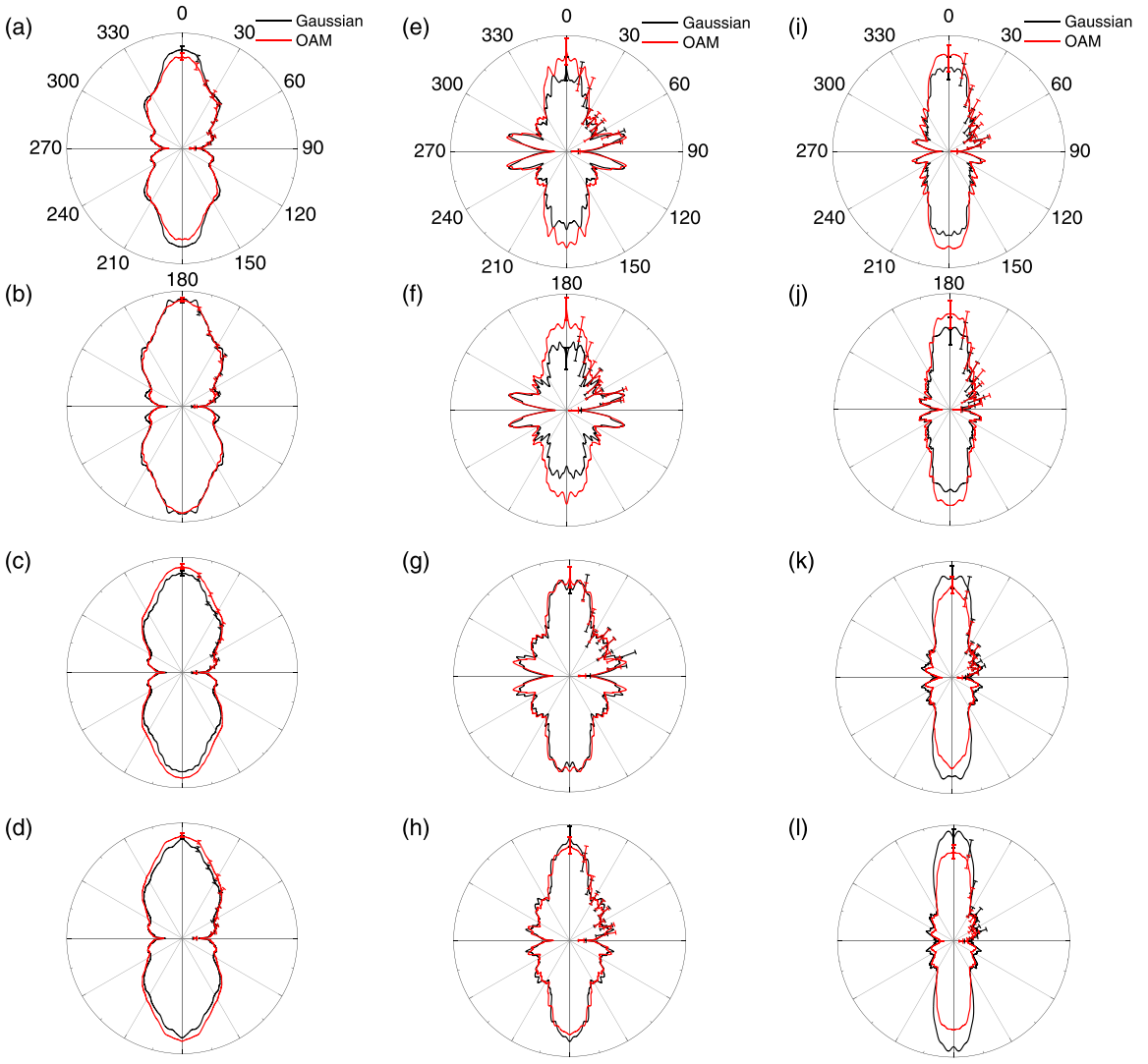

FIG. 6. The photoelectron angular distribution of the near-threshold photoelectrons from $HG_{0,0}$ (black) and $LG_{0,1}$ (red) beams is shown at different peak intensities [(a) 90 TW/cm^2, (b) 95 TW/cm^2, (c) 100 TW/cm^2, (d) 105 TW/cm^2]. Angular distributions of resonant photoelectrons with energy ∼0.7 eV [(e)–(h)] and ∼0.9 eV [(i)–(l)] are shown at the same intensities.

The PADs corresponding to the identified near-threshold ionization and resonant ionization processes are compared for $LG_{0,1}$ and $HG_{0,0}$ beams in Fig. 6. The kinetic energy of the nonresonant photoelectrons shifts towards the lower energy side with increasing peak intensity of the $LG_{0,1}$ field. The estimated intensity of the $LG_{0,1}$ laser pulse shows a good agreement with observed shift of the kinetic energy of the nonresonant photoelectrons. Within the error bars there is no distinguishable difference for the near-threshold electrons ionized by $HG_{0,0}$ or $LG_{0,1}$ beams. There are differences observable for the PADs for resonantly ionized electrons; however, there is no definite trend as a function of intensity, which we can identify in the range 90–105 TW/cm^2. The resonantly ionized electrons, for example, at lower laser intensities are relatively easier to be ionized by $LG_{0,1}$ beams, but this is not the case at slightly higher laser intensities. We must be careful in interpreting these because at higher laser intensities, the nonresonant ATI peak also overlaps with the resonant ATI peaks. This is particularly important as we consider Fig. 7.

In contrast to the resonant and near-threshold ionized electrons, the PAD of the nonresonant photoelectrons evidences a distinct suppression in ionization due to the $LG_{0,1}$ beams. This trend is true for both the nonresonant ATI electrons energies analyzed here and across the intensity regime sampled. With the electron energies shifting to lower energies with higher laser intensity, it is possible that the divergent behavior noted in the previous section for resonantly ionized electrons is due to a contribution from the nonresonant ATI electrons.

D. Discussion

According to theoretical studies addressing the interaction of a pulse beam carrying OAM with the simplest atom, hydrogen, new selection rules are expected:

$$|\Delta l| \leqslant |\ell| + 1 \tag{4}$$

for the laser pulse carrying OAM of the order ($\ell = 1$) [33]. Hence, one could expect a change in the angular distribution of these resonant photoelectrons for the same Rydberg states

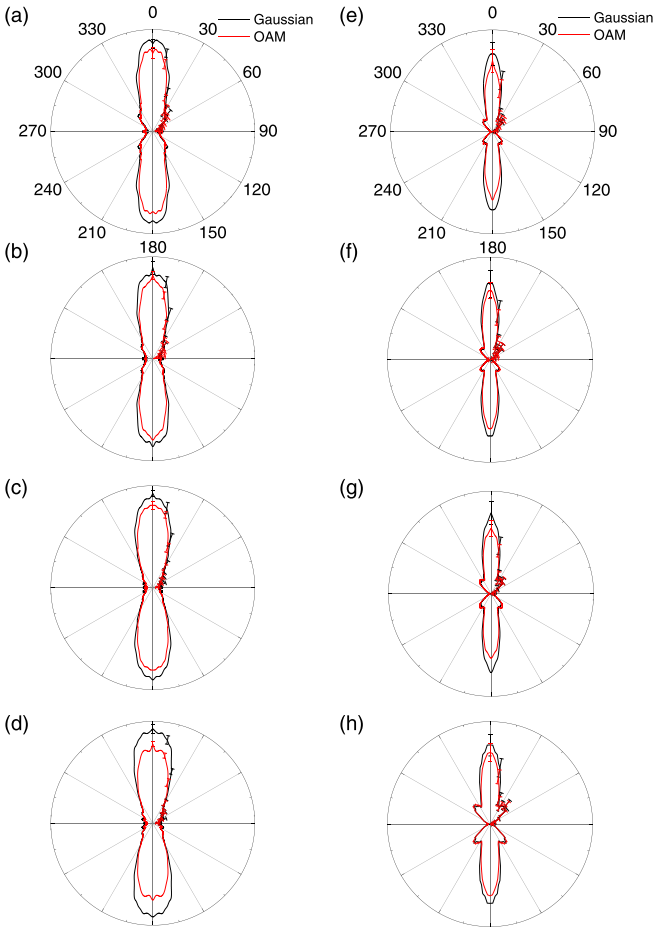

FIG. 7. Same as Fig. 6 but for the nonresonant photoelectrons at 1.85 eV and 3.4 eV at various peak intensities [(a, e) 90 TW/cm^2, (b, f) 95 TW/cm^2, (c, g)100 TW/cm^2, and (d, h)105 TW/cm^2].

are involved as in observed for the interaction with the Gaussian beam. However, the PAD of these resonant structures is not too divergent with the PAD seen in the interaction with Gaussian beams. The peaks in the angular distributions and even the partial wave components (not shown here) are not significantly different for the two cases.

This is not entirely unexpected as coupling of the OAM of light in the dipole approximation occurs only to the center-of-mass motion of the target system, and not to the internal motion as seen in experiments [30] and theory [58,59]. On the other hand, in the dark penumbra of the structured beams, strong excitation driven solely by the transverse field gradient, or quadrupole transitions, have been shown to exhibit OAM transfer. In a gas ensemble experiment, the target atoms randomly sample the focal volume. The observed signal, particularly from a nonlinear (in intensity) photoionization process, is dominated by atoms sampling the spatial regions of maximum intensity. So any significant change in selection rules and therefore differences in the PAD between $LG_{0,1}$ and $HG_{0,0}$ beams is not expected.

The angular distribution of the near-threshold photoelectrons is highly influenced by the Coulomb potential of the parent ion and the nature of the laser field. Hence, it is possible that, in the presence of the OAM-carrying laser field, electrons emerging from the ions close to the vortex of the beam may carry different angular momentum in the influence of a modified Coulomb potential due to the OAM beam. However, for the near-threshold electrons emerging from ions situated away from a vortex, the electron trajectory (order of sub-nm) remains unaffected by the intensity and phase structure of the OAM beam. Several theoretical studies have shown a significant change in the angular distribution due to the phase structure or to the intensity profile of the OAM beam only for the parent ions situated within a certain limit of the impact parameter $b < 100\ 000$ a.u. [35]. So for experimental measurements to observe the theoretically predicted effects due to the interaction with OAM beam close to the vortex would require an operational control of the impact parameter b. Such control could be achieved by future experiments using advanced atomic trap technology [60,61].

In contrast, the measured yield of the nonresonant ATI electron emission for $LG_{0,1}$ beams is consistently lower relative to that of $HG_{0,0}$ laser beams. The emission probability of these electrons is modulated in energy due to "interference in time." Essentially, in a strong-field picture (ignoring the effect of the atomic potential after ionization), the final drift momentum p_z in the laser polarization direction acquired by the electron is directly proportional to the rate of change of the electric field at the time the electron enters the laser field. So across multiple cycles of the laser field, electrons ionized at the same phase of the electric field emerge with the same momentum. Electrons with a certain p_z are therefore detected if the contributions from multiple cycles add constructively. With Gaussian beams the spatial extent of the interaction region is constrained, which is not the case for OAM beams. A possible consequence is that the contrast of the interference leading to the nonresonant ATI peaks is reduced. Alternately, an increased ionization volume for the $LG_{0,1}$ could also lead to an experimental observed broadening of the nonresonant ATI peaks, resulting in a decrease in their yield within a momentum window. Since each spectrum at each intensity is normalized to its total counts, the suppressed yields for the nonresonant ATI electrons for the $LG_{0,1}$ beams are reflected in the concomitant enhanced yields for the resonant peaks. With increasing intensity this is not so clear because the resonant ATI peaks overlap significantly, more so in the energy range of 1.0 ± 0.2 eV.

IV. SUMMARY

Angular momentum transfer from the structured light fields to internal degrees of freedom of a system through dipole interactions is not expected. However, experiments under strong-field conditions, limited to the generation of high harmonic radiation, provide evidence that the sum contributions over the extent of the target interfere to emboss a spatially varying phase over the high harmonic beams. The experiments detailed here compare the electron momentum distributions following strong-field ionization from laser beams with and without OAM. The results show no angular momentum transfer to the electrons in this regime (10^{13}–10^{14} W/cm^2, 800 nm). However, we have observed the yield of nonresonant ATI electrons for the case of $LG_{0,1}$ beams to be lower relative

to $HG_{0,0}$ beams. We speculate that this is primarily due to the increased spatial extent of the ionization volume in the case of $LG_{0,1}$. To conclusively prove that this is indeed the case, one needs to perform careful comparative experiments with a mixture of $LG_{0,1} + LG_{0,-1}$ beams. Such a beam would have the same spatial structure, but no OAM. From recent theoretical and experimental works that were carried out with two beams to investigate the influence of the OAM beam in an atomic system [45,46,62], the key to observe the modulation in the electronic wave packet by the OAM beam is to create an extended electronic wave packet in continuum-to-continuum transition so that the length scale of the electronic wave packet matches the gradient of the electric field associated with the OAM beam. Other beam experiments have to be designed to probe the properties of the "dark" section of the structured beams. For example, in a beam mixture $LG_{0,1} + HG_{0,0}$, with optimized intensities, it needs to be seen if OAM transfer to electrons can be effected.

The data that support the findings of this study are available from the corresponding author (V.S. and R.G) upon reasonable request.

ACKNOWLEDGMENTS

V.S. and R.G. thank Prof. M. Krishnamurthy for use of the laser facilities of the Tata Institute of Fundamental Research, Hyderabad, and for insightful suggestions. The funding from DST-SERB, DAE-BRNS, IMPRINT, UKIERI, and SPARC is gratefully acknowledged.

[1] P. Agostini, F. Fabre, G. Mainfray, G. Petite, and N. K. Rahman, Phys. Rev. Lett. **42**, 1127 (1979).
[2] L. V. Keldysh, Zh. Eksp. Teor. Fiz. **47**, 1945 (1964) [Sov. Phys. JETP **20**, 1307 (1965)].
[3] D. G. Arbo, S. Yoshida, E. Persson, K. I. Dimitriou, and J. Burgdorfer, Phys. Rev. Lett. **96**, 143003 (2006).
[4] Y. Huismans *et al.*,Science **331**, 61 (2011).
[5] R. R. Freeman, P. H. Bucksbaum, H. Milchberg, S. Darack, D. Schumacher, and M. E. Geusic, Phys. Rev. Lett. **59**, 1092 (1987)
[6] V. Schyja, T. Lang, and H. Helm, Phys. Rev. A **57**, 3692 (1998).
[7] A. Rudenko, K. Zrost, C. D. Schroter, V. L. B. de Jesus, B. Feuerstein, R. Moshammer, and J. Ullrich, J. Phys. B: At. Mol. Opt. Phys. **37**, L407 (2004).
[8] J. Burgdörfer, C. O. Reinhold, J. Sternberg, and J. Wang, Phys. Rev. A **51**, 1248 (1995).
[9] L. E. Cuéllar, C. S. Feigerle, H. S. Carman, Jr., and R. N. Compton, Phys. Rev. A **43**, 6437 (1991).
[10] K. Mitsuke, Y. Hikosaka, and K. Iwasaki, J. Phys. B: At. Mol. Opt. Phys. **33**, 391 (2000).
[11] C. I. Blaga, Nat. Phys. **5**, 335 (2009).
[12] K. L. Reid, D. J. Leahy, and R. N. Zare, Phys. Rev. Lett. **68**, 3527 (1992).
[13] C. Lux, Angew. Chem. Intl. Ed. Engl. **124**, 5086 (2012).
[14] T. Marchenko, H. G. Muller, K. J. Schafer, and M. J. Vrakking, J. Phys. B: At. Mol. Opt. Phys. **43**, 185001 (2010).
[15] H. G. Muller, P. H. Bucksbaum, D. W. Schumacher, and A. Zavriyev, J. Phys. B: At. Mol. Opt. Phys. **23**, 2761 (1990).
[16] G. Petite, P. Agostini, and F. Yergeau, J. Opt. Soc. Am. B **4**, 765 (1987).
[17] P. H. Bucksbaum, M. Bashkansky, R. R. Freeman, T. J. McIlrath, and L. F. DiMauro, Phys. Rev. Lett. **56**, 2590 (1986).
[18] R. Gopal, K. Simeonidis, R. Moshammer, T. Ergler, M. Durr, M. Kurka, K. U. Kuhnel, S. Tschuch, C. D. Schroter, D. Bauer *et al.*, Phys. Rev. Lett. **103**, 053001 (2009).
[19] D. Trabert, A. Hartung, S. Eckart, F. Trinter, A. Kalinin, M. Schöffler, L. Ph. H. Schmidt, T. Jahnke, M. Kunitski, and R. Dörner, Phys. Rev. Lett. **120**, 043202 (2018).
[20] L. Allen, M. W. Beijersbergen, R. J. C. Spreeuw, and J. P. Woerdman, Phys. Rev. A **45**, 8185 (1992).
[21] M. W. Beijersbergen, R. P. C. Coerwinkel, M. Kristensen, and J. P. Woerdman, Opt. Commun. **112**, 321 (1994).
[22] M. W. Beijersbergen, L. Allen, H. E. L. O. van der Veen, and J. P. Woerdman, Opt. Commun. **96**, 123 (1993).
[23] J. Arlt and K. Dholakia, Opt. Commun. **177**, 297 (2000).
[24] Y. Shen, X. Wang, Z. Xie, C. Min, X. Fu, Q. Liu, M. Gong, and X. Yuan, Light Sci. Appl. **8**, 90 (2019).
[25] L. Paterson, M. P. MacDonald, J. Arlt, W. Sibbett, P. E. Bryant, and K. Dholakia, Science **292**, 912 (2001).
[26] X. W. Zhuang, Science **305**, 188 (2004).
[27] M. Harwit, Astrophys. J. **597**, 1266 (2003).
[28] S. Fürhapter, A. Jesacher, S. Bernet, and M. Ritsch-Mart, Opt. Express **13**, 689 (2005).
[29] F. Tamburini, G. Anzolin, G. Umbriaco, A. Bianchini, and C. Barbieri, Phys. Rev. Lett. **97**, 163903 (2006).
[30] F. Giammanco, A. Perona, P. Marsili, F. Conti, F. Fidecaro, S. Gozzini, and A. Lucchesini, Opt. Lett. **42**, 219 (2017).
[31] A. Muthukrishnan and C. R. Stroud, Jr., J. Opt. B: Quantum Semiclass. Opt. **4**, S73 (2002).
[32] C. T. Schmiegelow, J. Schulz, H. Kaufmann, T. Ruster, U. G. Poschinger, and F. Schmidt-Kaler, Nat. Commun. **7**, 12998 (2016).
[33] A. Picón, J. Mompart, J. R. Vázquez de Aldana, L. Plaja, G. F. Calvo, and L. Roso, Opt. Express **18**, 3660 (2010).
[34] A. Picón, A. Benseny, J. Mompart, J. R. Vázquez de Aldana, L. Plaja, G. F. Calvo, and L. Roso, New J. Phys. **12**, 083053 (2010)
[35] O. Matula, A. Hayrapetyan, V. G. Serbo, A. Surzhykov, and S. Fritzsche, J. Phys. B: At. Mol. Opt. Phys. **46**, 205002 (2013).
[36] W. Paufler, B. Böning, and S. Fritzsche, Phys. Rev. A **97**, 043418 (2018).
[37] B. Böning, W. Paufler, and S. Fritzsche, Phys. Rev. A **98**, 023407 (2018).
[38] P. C. Deshmukh, E. Krishnakumar, Stephan Fritzsche, M. Krishnamurthy, and S. Majumder (Eds.), in *Quantum Collisions and Confinement of Atomic and Molecular Species, and Photons, Select Proceedings of the 7th Topical Conference of ISAMP 2018*, 1st ed., Springer Proceedings in Physics (SPPHY), Vol. 230 (Springer, Singapore, 2019), p. 284.
[39] T. Ruchon, C. Chappuis, R. Géneaux, D. Bresteau, O. Gobert, G. de Ninno, D. Gauthier, and T. Auguste, in *Conference on Lasers and Electro-Optics Europe* (Optica Publsihing Group, 2019).
[40] W. Paufler, B. Böning, and S. Fritzsche, J. Opt. **21**, 094001 (2019).

[41] C. Hernández-García, J. San Román, L. Plaja and A. Picón, New J. Phys. **17**, 093029 (2015).
[42] D. Gauthier, P. Ribič, G. Adhikary *et al.*, Nat. Commun. **8**, 14971 (2017).
[43] C. Hernández-García, A. Picón, J. San Román, and L. Plaja, Phys. Rev. Lett. **111**, 083602 (2013).
[44] K. Amini, A. Chaćon, S. Eckart, B. Fetíc, and M. Kübel, Eur. Phys. J. D **75**, 275 (2021).
[45] G. De Ninno *et al.*, Nat. Photonics **14**, 554 (2020).
[46] Y. Fang, Z. Guo, Peipei Ge, Y. Dou, Y. Deng, Q. Gong, and Y. Liu, Light Sci. Appl. **11**, 34 (2022).
[47] S. N. Alperin, R. D. Niederriter, J. T. Gopinath, and M. E. Siemens, Opt. Lett. **41**, 5019 (2016).
[48] J. Ullrich, R. Moshammer, A. Dorn, R. Dörner, L. Ph. H. Schmidt, and H. Schmidt-Böcking, Rep. Prog. Phys. **66**, 1463 (2003).
[49] R. Gopal, Electron wave packet interferences in ionization with few-cycle laser pulses and the dissociative photoionization of D_2 with ultrashort extreme ultraviolet pulses, Ph.D. thesis, Combined Faculties for the Natural Sciences and for Mathematics of the Ruperto-Carola University of Heidelberg, Germany (2010), doi: 10.11588/heidok.00010638, pp. 68–69.
[50] M. Li, P. Zhang, S. Luo, Y. Zhou, Q. Zhang, P. Lan, and P. Lu, Phys. Rev. A **92**, 063404 (2015).
[51] https://physics.nist.gov/cgi-bin/ASD/energy1.pl.
[52] Z. Chen, T. Morishita, A.-T. Le, M. Wickenhauser, X. M. Tong, and C. D. Lin, Phys. Rev. A **74**, 053405 (2006).
[53] C. A. Mancuso, K. M. Dorney, D. D. Hickstein, J. L. Chaloupka, X.-M. Tong, J. L. Ellis, H. C. Kapteyn, and M. M. Murnane, Phys. Rev. A **96**, 023402 (2017).
[54] S. Eckart, D. Trabert, K. Fehre, A. Geyer, J. Rist, K. Lin, F. Trinter, L. Ph. H. Schmidt, M. S. Schöffler, T. Jahnke, M. Kunitski, and R. Dörner, Phys. Rev. A **102**, 043115 (2020).
[55] M. Li, Y. Liu, H. Liu, Y. Yang, J. Yuan, X. Liu, Y. Deng, C. Wu, and Q. Gong, Phys. Rev. A **85**, 013414 (2012).
[56] D. G. Arbó, K. I. Dimitriou, E. Persson, and J. Burgdörfer, Phys. Rev. A **78**, 013406 (2008).
[57] M. Schuricke, G. Zhu, J. Steinmann, K. Simeonidis, I. Ivanov, A. Kheifets, A. N. Grum-Grzhimailo, K. Bartschat, A. Dorn, and J. Ullrich, Phys. Rev. A **83**, 023413 (2011).
[58] M. Babiker, C. R. Bennett, D. L. Andrews, and L. Dávila Romero, Phys. Rev. Lett. **89**, 143601 (2002).
[59] P. K. Mondal, B. Deb, and S. Majumder, Phys. Rev. A **89**, 063418 (2014).
[60] M. A. Wilson, P. Bushev, J. Eschner, F. Schmidt-Kaler, C. Becher, R. Blatt, and U. Dorner, Phys. Rev. Lett. **91**, 213602 (2003).
[61] B. Murphy and L. Vestergaard Hau, Phys. Rev. Lett. **102**, 033003 (2009).
[62] B. Baghdasaryan, B. Böning, W. Paufler, and S. Fritzsche, Phys. Rev. A **99**, 023403 (2019).